

EXERGY AND INTEGRAL BOUNDARY LAYER PARAMETERS CHARACTERISTIC CURVES FOR AERODYNAMIC DESIGN AND OPTIMIZATION

Guillaume Bourreau-Tirel [1,2], Sébastien Duplaa [2] & Juan Pablo Ruscio[1]

[1]Aura Aero, 31270, Toulouse, France
guillaume.bourreautirel@aura-aero.com, juanpablo.ruscio@aura-aero.com

[2]ISAE-Supaéro, Toulouse University, 31055, Toulouse, France
Sebastien.DUPLAA@isae.fr

Abstract

Exergy analysis provides a quantification of the energy recovery potential valuable for aircraft design. Recent developments have introduced an exergy-based formulation for profile drag study specifically dedicated to low-fidelity simulations input data. This approach is substantially less computationally demanding than the higher-fidelity simulations previously required for such analyses, while demonstrating satisfactory accuracy for conceptual design phases. The current work aims to explore the design space of this low-fidelity method by establishing its characteristic curves to assess the general relations and sensitivities of exergy parameters relative to classical Integral Boundary Layer (IBL) quantities. Additionally, exergy-based distributions computed along the LS0417 airfoil family are superimposed on these maps to illustrate how this framework serves as a valuable conceptual design tool for power recovery potential evaluation. A novel low-fidelity, exergy-driven airfoil optimization methodology based on a genetic algorithm is also implemented and applied to the redesign of the NACA 2414 airfoil, demonstrating the capability to improve the recoverable energy potential at a targeted spatial region of a given geometry while maintaining global aerodynamic loads.

Keywords: Thermodynamics, Entropy, Airfoil Optimization, Conceptual Design, Profile Drag

1. Introduction

Exergy analysis has emerged as a rigorous thermodynamic framework to evaluate aerodynamic performance and quantify the power saving benefits of airframe-propulsion integration. While recent developments have demonstrated the significant value of this approach [1], [2], [3], [4], they rely on mid-fidelity Reynolds-Averaged Navier-Stokes (RANS) simulations. The computational expense and complex volume mesh generation associated with RANS solvers remain prohibitive for extensive design space exploration and integration into Multidisciplinary Design Analysis and Optimization (MDAO) loops at the conceptual stage. Consequently, rapid low-fidelity tools based on surface meshes and Integral Boundary Layer (IBL) equations, such as viscous-coupled panel methods, remain widely used in the industry. To bridge this gap, the authors previously developed a low-fidelity exergy-based method for 2D attached subsonic flows [5] which demonstrated excellent agreement with higher-fidelity references [1], [2].

By bypassing the complexities of automated volume meshing and reducing computational cost, this low-fidelity exergy method unlocks new capabilities for conceptual design. It serves as an efficient, easily implementable tool for comprehensive design space exploration and automated optimization loops. Building upon this foundation, the present article aims to systematically determine the general relationships between a given boundary layer state described by classical IBL quantities and its associated exergy parameters. To this end, exergy and IBL characteristic curves are established to map

https://doi.org/10.71945/icas2026_0378

this thermodynamic design space, providing a valuable tool for propulsive integration evaluation of a wide range of geometries (e.g., airfoils, fuselages). Finally, the practical application of this framework is demonstrated through the development and implementation of a novel low-fidelity exergy-driven shape optimization process applied to a 2D airfoil.

2. Low-fidelity exergy method for profile drag analysis

This section summarizes the equations and methodology of the 2D low-fidelity exergy-based formulation for profile drag assessment introduced in [5]. The method is applicable to steady, compressible, subsonic, adiabatic and attached flows. It relies on the velocity decomposition proposed by Aguirre [2] as an extension of Arntz's original formulation [1], which separates the flow into inviscid (isentropic) and viscous (non-isentropic) components, combined with the thin boundary layer approximation. Under these hypotheses, viscous mechanical exergy ($\bar{\dot{\varepsilon}}_m = \bar{\dot{E}}_u + \bar{\dot{E}}_v + \bar{\dot{E}}_p$), thermal exergy ($\bar{\dot{\varepsilon}}_{th}$), and anergy ($\dot{\mathscr{A}}$) constitute the exergy-based viscous drag $C_{D_{\bar{\varepsilon}}}$ (relative to profile drag), as defined in Eq.(1). These quantities are here expressed, adapted to a low-fidelity formalism, as functions of boundary layer integral quantities, local edge conditions ($U_e, P_{S,e}, T_{S,e}$), and the geometric angle ϕ between aerodynamic and local boundary layer frames, through Eqs.(2)–(6):

$$C_{D_{\bar{\varepsilon}}} = C_{D_\varepsilon} - C_{D_{\varepsilon^*}} = \frac{\bar{\dot{\varepsilon}}_m + \bar{\dot{\varepsilon}}_{th} + \dot{\mathscr{A}}}{\frac{1}{2}\,\rho_0 u_0^3\, S_{ref}} \tag{1}$$

$$\bar{\dot{E}}_u = -\frac{K}{2}\cos^4\phi - \frac{M}{2}(U_e^2\cos^4\phi + u_0^2\cos^2\phi) + u_0(k + U_e^2 m)\cos^3\phi \tag{2}$$

$$\bar{\dot{E}}_v = -\frac{1}{2}(K + U_e^2 M)\sin^2\phi\cos^2\phi \tag{3}$$

$$\bar{\dot{E}}_p = -P_{S_e} Q\cos^2\phi + \frac{P_{S_0}}{\rho_0}\left(M\left[1 + \ln\left(\frac{\rho_0}{\rho_e}\right)\right] - C\right)\cos^2\phi \tag{4}$$

$$\bar{\dot{\varepsilon}}_{th} = -c_v E\cos^2\phi + c_v T_{S_0}\left(M\left[1 + \ln\left(\frac{T_{S_e}}{T_{S_0}}\right)\right] + E'\right)\cos^2\phi \tag{5}$$

$$\dot{\mathscr{A}} = T_{S_0}\int_0^\delta \rho c_p \ln\left[\left(\frac{P_{Se}}{P_{S_0}}\right)^{\frac{1-\gamma}{\gamma}}\left(1 + \frac{(\gamma-1)}{2}M_0^2\left(1 - \frac{U^2}{u_0^2}\right)\right)\right] U\cos^2\phi\, dn \tag{6}$$

Using the following boundary layer integral defects and their corresponding thicknesses:

$$\begin{aligned}
K &= \rho_e U_e^3\theta^* = \int_0^\delta (U_e^2 - U^2)\rho U dn & M &= \rho_e U_e \delta^* = \int_0^\delta (\rho_e U_e - \rho U) dn \\
k &= \rho_e U_e^2 \theta'^* = \int_0^\delta (U_e^2 - U^2)\rho dn & m &= \rho_e \delta'^* = \int_0^\delta (\rho_e - \rho) dn \\
Q &= U_e\delta_V = \int_0^\delta (U_e - U) dn & C &= \rho_e U_e \delta_C = \int_0^\delta \ln\left(\frac{\rho_e}{\rho}\right)\rho U dn \\
E &= \rho_e T_{S_e} U_e \delta_E = \int_0^\delta (\rho_e T_{S_e} U_e - \rho T_S U) dn & E' &= \rho_e U_e \delta_{E'} = \int_0^\delta \ln\left(\frac{T_{S_e}}{T_S}\right)\rho U dn
\end{aligned} \tag{7}$$

Since the viscous coupling procedure in low-fidelity panel solvers typically provides only a limited set of integral parameters (θ, H, δ, U_e), an intermediate reconstruction step is necessary. On the body surface, boundary layer velocity profiles are reconstructed using Falkner-Skan self-similar solutions for laminar regions and the Swafford wall function for turbulent ones. In turbulent wake regions, an adaptation of Coles's law is employed, while density and temperature profiles are obtained from the Crocco-Busemann relation. This approach enables the computation of all integral defects (K, M, k, m, Q, C, E, E') required by the low-fidelity exergy formulation. The overall computational procedure associated with the low-fidelity exergy methodology is depicted in Figure 1.

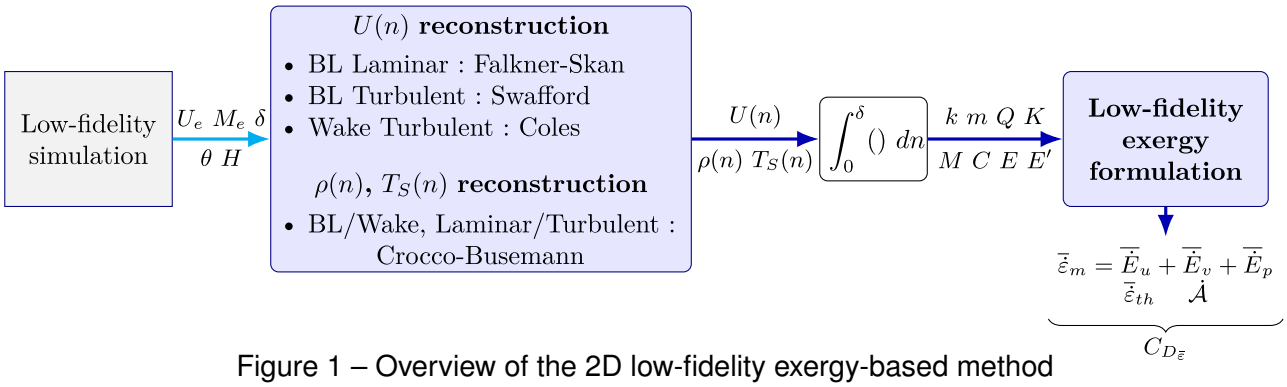


Figure 1 – Overview of the 2D low-fidelity exergy-based method

3. Exergy and IBL parameters characteristic curves

This section details the construction of the characteristic curves (Figs. 3, 4, 6) derived from the low-fidelity exergy framework introduced previously. By systematically sweeping the primary IBL input parameters and computing the corresponding exergy metrics, the design space is thoroughly explored within the formulation's domain of validity.

To exhaustively cover all possible states of attached boundary layers on an arbitrary geometry, the parametric sweep is performed over three dimensionless variables: M_e/M_0, H_k, and Re_θ. These latter two IBL parameters are fully expressed as functions of the variables typically provided by low-fidelity viscous-coupled panel method simulations (and even directly output by XFoil software [6]), and are defined as:

$$H_k = \frac{H - 0.29M_e^2}{1 + 0.113M_e^2} \quad H \equiv \frac{\delta^*}{\theta} \quad , \quad Re_\theta \equiv \frac{U_e\,\theta}{\nu} \quad \text{where} \quad \delta^* \equiv \int_0^\delta (1 - \frac{\rho U}{\rho_e U_e})\, dn \quad \theta \equiv \int_0^\delta (1 - \frac{\rho U}{\rho_e U_e}) \frac{\rho U}{\rho_e U_e}\, dn \quad (8)$$

It is worth noting that the classical displacement thickness δ^* and momentum thickness θ are not computed in practice by integrating detailed velocity and density profiles, as these are not explicitly resolved in low-fidelity codes. Instead, they are directly derived from the scalar von Kármán integral equation solved within the panel method's viscous-inviscid coupling procedure.

Here, the kinematic shape factor H_k is the equivalent incompressible shape factor (defined assuming a constant density across the boundary layer). It is related to the compressible shape factor H by the correlation derived by Whitfield [7] for adiabatic airflows (first expression in Eq. 8). Physically, H_k characterizes the boundary layer velocity profile shape, which results from the pressure gradient history along the geometry. Low values of H_k indicate a strongly attached boundary layer driven by a favorable pressure gradient, whereas higher values correspond to profiles approaching separation. Re_θ is the Reynolds number based on the momentum thickness θ. It indicates the spatial extent of the boundary layer domain, thereby quantifying the scale of the local momentum defect. Lastly, M_e/M_0 represents the ratio of the local boundary layer edge Mach number to the freestream value. It determines whether the flow is locally accelerated or decelerated, and is thus directly related to the local pressure coefficient C_p.

The exergy characteristic curves are constructed by sweeping H_k (reported on the abscissa in Figs. 3, 4, 6) while plotting curves of constant Re_θ and M_e/M_0. To maintain a strictly constant Re_θ for each M_e/M_0 ratio, the momentum thickness θ is adjusted to compensate for the change in edge Mach number.

For each set of $(M_e/M_0, H_k, Re_\theta)$, the corresponding exergy-based values are calculated following the computational framework outlined in Fig. 1. The resulting exergy characteristic curves include the exergy-based viscous drag ($C_{D_{\bar{\varepsilon}}}$), which corresponds to the profile drag. This term is further decomposed into anergy ($\dot{\mathscr{A}}$, the irrecoverable part) and viscous mechanical and thermal exergy ($\bar{\varepsilon}_m$ and $\bar{\varepsilon}_{th}$, the recoverable portions). All these quantities are expressed in power counts ($1\ \text{pc} = 10^{-4}$), equivalent to classical drag counts (dc), while the Exergy Waste Coefficient, $EWC = \frac{\bar{\varepsilon}_m + \bar{\varepsilon}_{th}}{\bar{\varepsilon}_m + \bar{\varepsilon}_{th} + \dot{\mathscr{A}}}$, quantifies the fraction of the profile drag that is potentially recoverable from a thermodynamic perspective and is given in %. The characteristic curves are depicted in Figs. 3, 4, and 6 as grey lines without markers. These results are obtained for a freestream Mach number $M_0 = 0.3$, fixing the freestream velocity u_0 involved in Eqs. 2 to 6, with all exergy-based power quantities non-dimensionalized by $\frac{1}{2}\rho_0 u_0^3$.

This general approach is conceptually similar to the dissipation coefficient ($c_{\mathscr{D}}$) maps introduced in Drela's power balance method [8, 9], which depict the mechanical energy dissipation coefficient against H and Re_θ, as reproduced in Fig. 2.

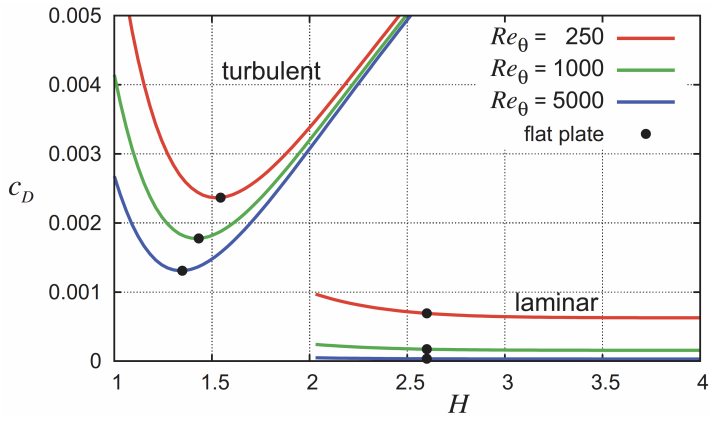
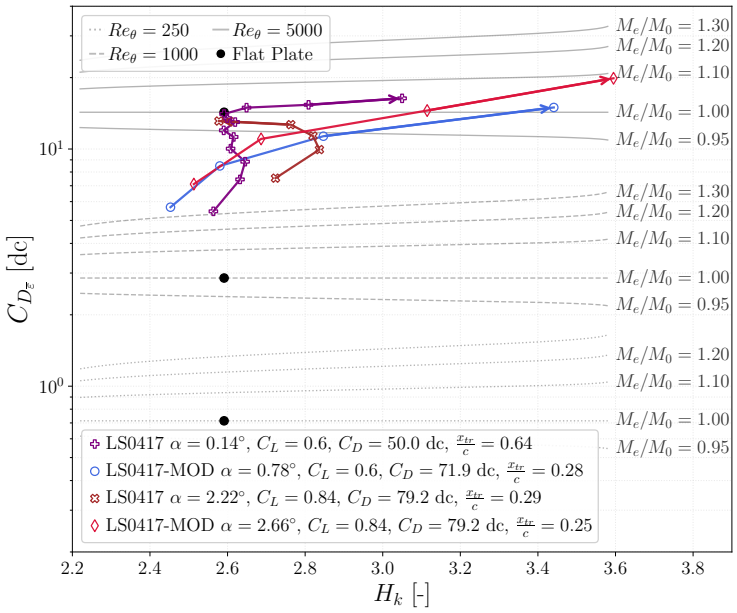


Figure 2 – Dissipation coefficient from self-similar laminar and turbulent flow (adapted from [9]).

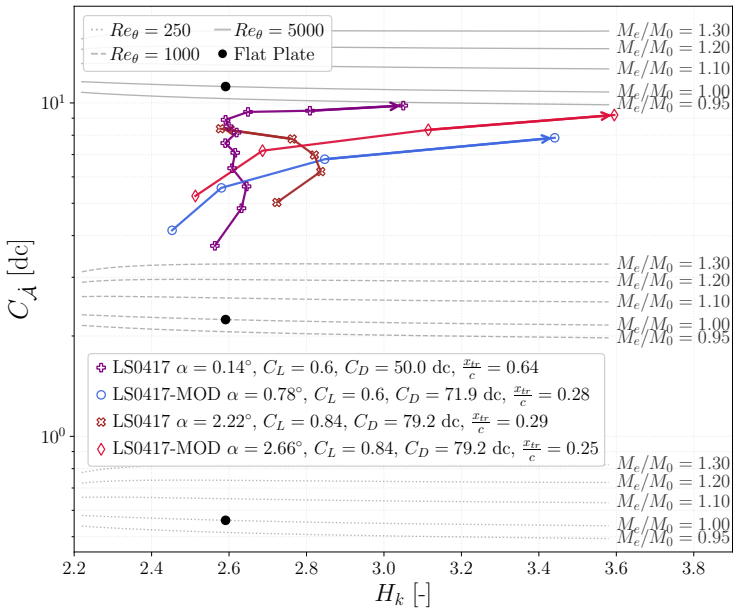
However, while the power balance method quantifies total mechanical energy dissipation, it does not distinguish between its recoverable and non-recoverable components. In contrast, the current exergy-based framework identifies the fraction of profile drag that can potentially be recovered (viscous exergy) versus the portion definitively lost through irreversible processes (anergy). Consequently, the mapping presented herein offers additional physical insight into the thermodynamic performance of the boundary layer by providing the overall dependence of exergy-based parameters on classical IBL quantities. Beyond providing a new method for profile drag prediction, it serves as a valuable tool for conceptual design, particularly for evaluating the energy recovery benefits of airframe-propulsion integration, such as Boundary Layer Ingestion (BLI) configurations.
The following subsections analyze these exergy-based characteristic curves for laminar and turbulent boundary layers, as well as turbulent wakes. This approach encompasses a wide range of flow conditions, allowing for the consideration of both transitional and fully turbulent aerodynamic configurations.

3.1 Laminar Boundary Layer

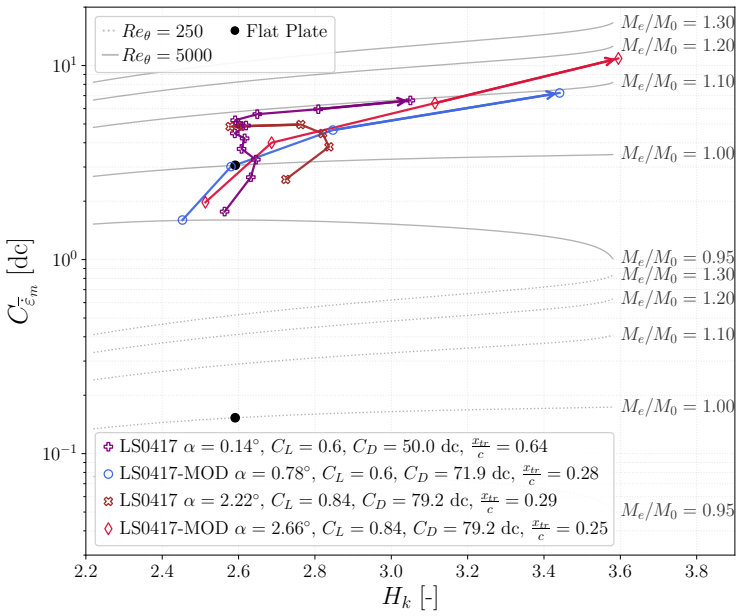
First, the exergy characteristic curves for laminar boundary layers, derived from Falkner-Skan self-similar profiles, are presented in Fig. 3. The analysis is explicitly restricted to attached boundary layers, thereby limiting the kinematic shape factor (H_k) to a range between 2.22 and 3.6. The selected momentum thickness Reynolds numbers ($Re_\theta = 250$, 1000, and 5000) are representative of the laminar regions on transitional airfoils operating at high Reynolds numbers, typical of subsonic civil aircraft in cruise flight. Finally, the displayed edge-to-freestream Mach number ratios (M_e/M_0 ranging from 0.95 to 1.3) encompass the typical accelerated and decelerated flow states encountered along these airfoils under such operational conditions.
As observed in Figs. 3a, 3b, and 3c, the iso-M_e/M_0 curves for $\overline{\dot{\varepsilon}}_m$, $\dot{\mathscr{A}}$, and $C_{D_{\bar{\varepsilon}}}$ scale strictly with Re_θ throughout the considered range of H_k. Consequently, these exergy-based quantities are directly proportional to the momentum thickness, θ. This scaling is physically expected since Re_θ quantifies the magnitude of the boundary layer development through its momentum deficit, which directly governs the profile drag level.
Furthermore, the values of $\overline{\dot{\varepsilon}}_m$, $\dot{\mathscr{A}}$, and $C_{D_{\bar{\varepsilon}}}$ increase with higher M_e/M_0 ratios, implying that highly accelerated flow regions along a given geometry generate substantial local profile drag. This trend aligns with Drela's analysis [9], which highlights that kinetic energy dissipation is proportional to U_e^3 (the cube of the boundary layer edge velocity).
For any given Re_θ, along an iso-M_e/M_0 curve, $C_{D_{\bar{\varepsilon}}}$ exhibits a roughly linear dependence on H_k. The slope of this variation depends on the local Mach value (linked to local C_p value): it is positive for accelerated flows ($M_e/M_0 > 1$) and negative for decelerated flows ($M_e/M_0 < 1$). A similar behavior is observed for the viscous mechanical exergy, $\overline{\dot{\varepsilon}}_m$, which grows with H_k when $M_e/M_0 \geq 1$ but slightly



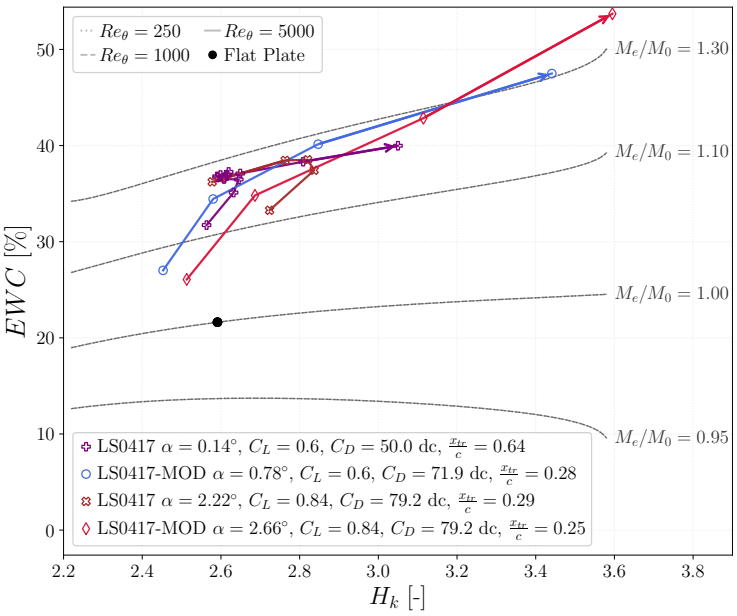
(a) Exergy-based viscous drag



(b) Anergy



(c) Viscous mechanical exergy



(d) Exergy Waste Coefficient

Figure 3 – Characteristic exergy/IBL curves for laminar attached boundary layers at $M_0 = 0.3$ and upper-surface exergy-based distributions for fully turbulent airfoils at $M_0 = 0.3$, $R_e = 3 \times 10^6$

decreases under decelerated conditions (e.g., the $M_e/M_0 = 0.95$ curve). As shown in Fig. 3b, the anergy $\dot{\mathscr{A}}$ remains largely insensitive to H_k (showing only a slight decline), with a gradient that appears unaffected by the Mach ratio. This relative independence from the shape factor mirrors the behavior of the kinetic energy dissipation coefficient ($c_{\mathscr{D}}$) evidenced by Drela for laminar flows, as visible in Fig. 2.

These trends result in an Exergy Waste Coefficient (EWC), shown in Fig. 3d, that is independent of Re_θ. The EWC rises monotonically with M_e/M_0 and, along a constant Mach ratio contour, increases with H_k for $M_e/M_0 > 1$ while decreasing for $M_e/M_0 < 1$. This indicates that locally accelerated boundary layers and those approaching separation contain the highest proportion of viscous exergy relative to the overall profile drag generated. Therefore, they offer the most significant opportunity for energy recovery. Figure 3d indicates that the profile drag associated with accelerated laminar regions, such as those preceding transition on the upper surface of an airfoil, comprises a substantial recoverable

fraction, typically reaching 30% to 40%.
Additionally, reference points for the flat plate boundary layer, computed at various Re_θ values under zero-pressure-gradient conditions (i.e., $M_e/M_0 = 1$ with the classical Falkner-Skan shape factor $H_k = 2.59$), are superimposed on these maps. The corresponding proportion of recoverable viscous exergy, indicated by an EWC of 21.6% in Fig. 3d, is in excellent agreement with the 21.4% value obtained with the Blasius solution reported by Drela [8].

3.2 Turbulent Boundary Layer

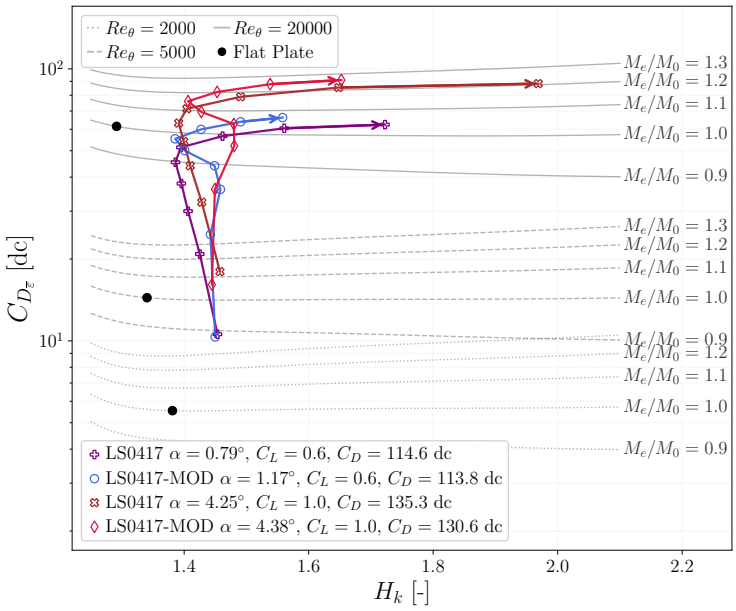
Turning to the turbulent regime, the corresponding exergy characteristic curves, computed using the Swafford velocity profile reconstruction, are presented in Fig. 4. The analysis focuses on attached turbulent flows, bounding the kinematic shape factor (H_k) between 1.25 and 2.1. Once again, the selected momentum thickness Reynolds numbers ($Re_\theta = 2000$, 5000, and 20000) and the edge-to-freestream Mach ratios (M_e/M_0 ranging from 0.9 to 1.3) cover the typical boundary layer development and pressure gradients found along fully turbulent aircraft wings at cruise.
Flat plate reference points for the different Re_θ are also overlaid on these maps. To determine the equilibrium kinematic shape factor for a zero-pressure-gradient turbulent flat plate (denoted here as $H_k(\beta = 0)$), which, unlike the laminar case, varies with Re_θ, a skin friction model is combined with the Clauser equilibrium parameters $G - \beta$ [10]. In the present approach, the skin friction coefficient, C_f, is evaluated using Swafford's correlation [11]. The latter accounts for compressibility effects via Whitfield's transformation, relating the equivalent incompressible skin friction, $F_c C_f$, to H_k and Re_θ through:

$$F_c C_f = 0.3e^{-1.33H_k}\left[\log_{10}\left(\frac{Re_\theta}{F_c}\right)\right]^{-1.74-0.31H_k} + 0.00011\left[\tanh\left(4-\frac{H_k}{0.875}\right)-1\right] \tag{9}$$

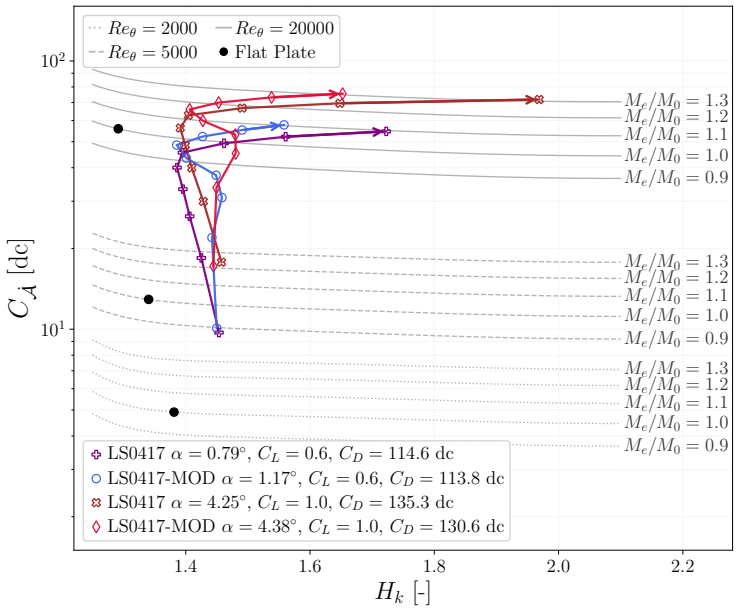
where the adiabatic compressibility factor is defined as $F_c = \sqrt{1+0.2M_e^2}$.
Applying the semi-empirical $G - \beta$ locus relation of Clauser [10] under zero-pressure-gradient conditions ($G(\beta = 0) \simeq 6.7$) yields the following implicit equation for $H_k(\beta = 0)$:

$$H_k(\beta=0) = \frac{1}{1-6.7\sqrt{\frac{F_c C_f(H_k(\beta=0),\, Re_\theta,\, \frac{M_e}{M_0}=1)}{2}}} \tag{10}$$

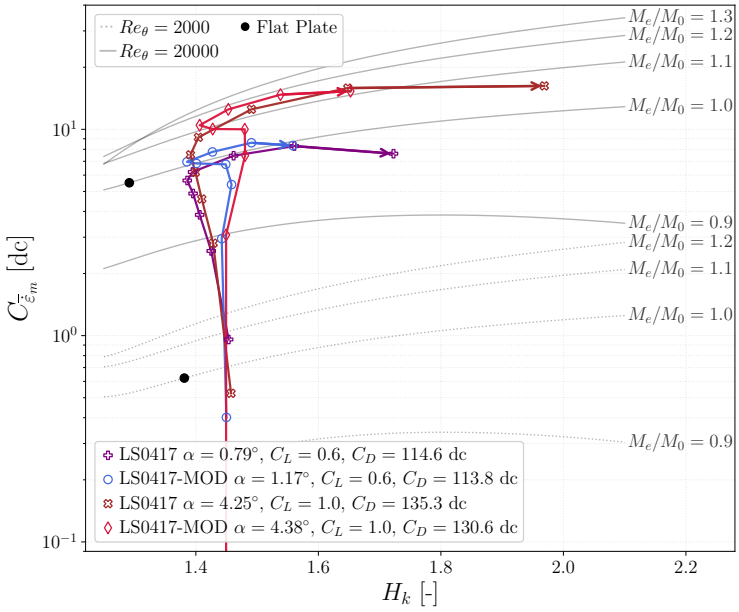
Solving this equation by employing Eq. 9 yields $H_k(\beta = 0)$, which decreases at higher Re_θ as observed in Fig. 4 (a trend consistent with the turbulent flat plate H_k values presented in Fig. 2).
Figures 4a, 4b, and 4c present the characteristic curves for $C_{D_{\bar{\varepsilon}}}$, $\dot{\mathscr{A}}$, and $\overline{\dot{\varepsilon}}_m$. Globally, these quantities exhibit greater magnitudes than in the laminar regime, reflecting the inherently higher profile drag produced by turbulent flows. Similar to the laminar analysis, the iso-M_e/M_0 contours still largely scale with Re_θ. More precisely, while $\overline{\dot{\varepsilon}}_m$ remains directly proportional to Re_θ across the entire examined H_k range, $\dot{\mathscr{A}}$ and the resulting $C_{D_{\bar{\varepsilon}}}$ follow this scaling primarily for $H_k \gtrsim 1.6$. Below this threshold ($H_k < 1.6$), both the anergy and the exergy-based viscous drag coefficient become comparatively higher at greater momentum thickness Reynolds numbers.
As in the laminar case, $\overline{\dot{\varepsilon}}_m$, $\dot{\mathscr{A}}$, and $C_{D_{\bar{\varepsilon}}}$ all increase with the boundary layer edge Mach ratio, M_e/M_0. Furthermore, along the iso-M_e/M_0 curves, $\overline{\dot{\varepsilon}}_m$ grows monotonically for accelerated flows ($M_e/M_0 > 1$). In contrast, under decelerated conditions (as seen for $M_e/M_0 = 0.9$), it initially rises to a peak near $H_k \approx 1.7$ before declining at higher shape factors, as depicted in Fig. 4c. Meanwhile, anergy levels globally decrease as H_k increases. This decline is more pronounced at low H_k values, which is attributed to the greater near-wall velocity gradients associated with strongly attached flows, generating more entropy.
These opposing behaviors of viscous exergy and anergy yield non-monotonic characteristic curves for $C_{D_{\bar{\varepsilon}}}$. Specifically, for accelerated cases ($M_e/M_0 > 1$), this exergy-based profile drag coefficient reaches a minimum located close to the zero-pressure-gradient flat plate H_k value. This evolution closely mirrors the one evidenced by Drela for the turbulent dissipation coefficient, which similarly exhibits a minimum near the flat plate condition, as visible in Fig. 2. The thermodynamic approach adopted here provides an additional physical insight: below this $H_{k_{min}}$ threshold, profile drag generation consists predominantly of anergy. Above $H_{k_{min}}$, the overall profile drag growth is driven by the viscous mechanical exergy, which increases more rapidly than the anergy decreases.



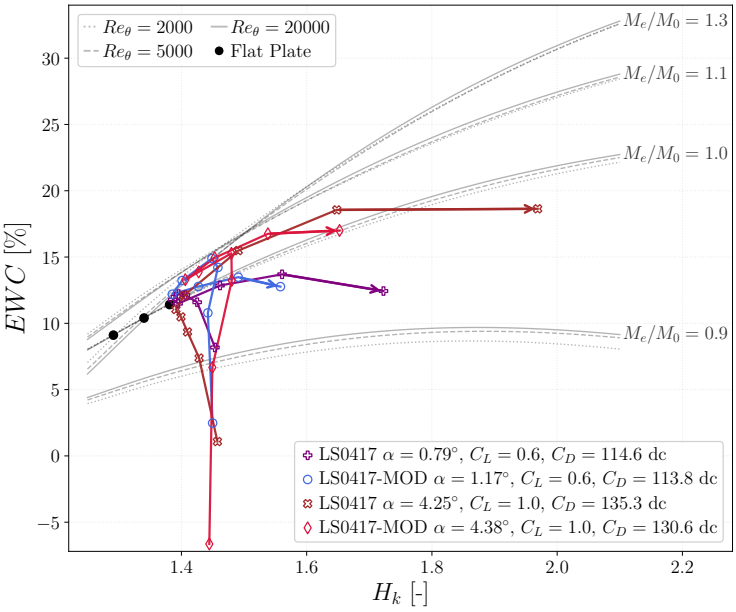
(a) Exergy-based viscous drag



(b) Anergy



(c) Viscous mechanical exergy



(d) Exergy Waste Coefficient

Figure 4 – Characteristic exergy/IBL curves for turbulent attached boundary layers at $M_0 = 0.3$ and upper-surface exergy-based distributions for fully turbulent airfoils at $M_0 = 0.3$, $R_e = 3 \times 10^6$

The recoverable energy fraction of profile drag is quantified by the EWC levels plotted in Fig. 4d. Regarding the flat plate reference points, the EWC values decrease slightly as Re_θ increases, remaining near 10%. This indicates that turbulent boundary layers possess roughly half the energy recovery potential of laminar ones. This baseline value is consistent with a previous study by the authors [12] and the results of Lamprakis [13].

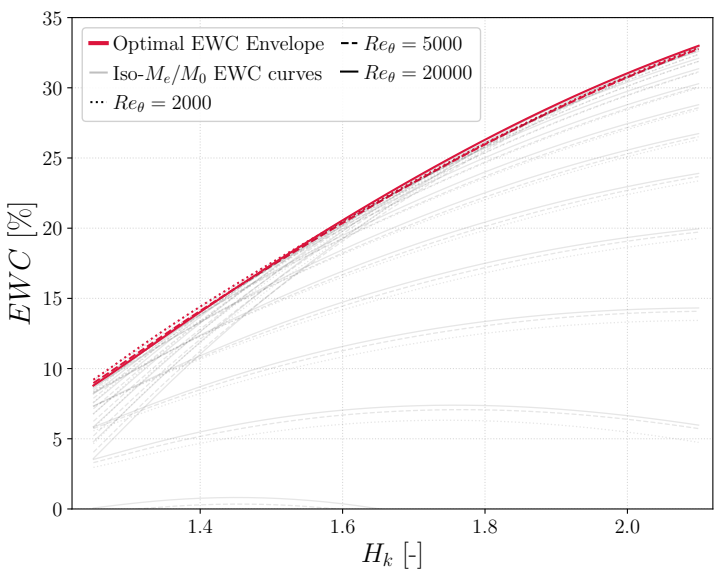
Notably, the EWC is nearly independent of Re_θ and increases with H_k with a gradient proportional to the Mach ratio (M_e/M_0).

Furthermore, an interesting feature of the turbulent regime, which differs from the laminar case, is that the EWC does not scale monotonically with M_e/M_0. Consequently, the most accelerated flows (i.e., those with the highest M_e/M_0 values) do not systematically yield the highest EWC. This is clearly visible in Fig. 4d, where the iso-M_e/M_0 contours intersect one another.

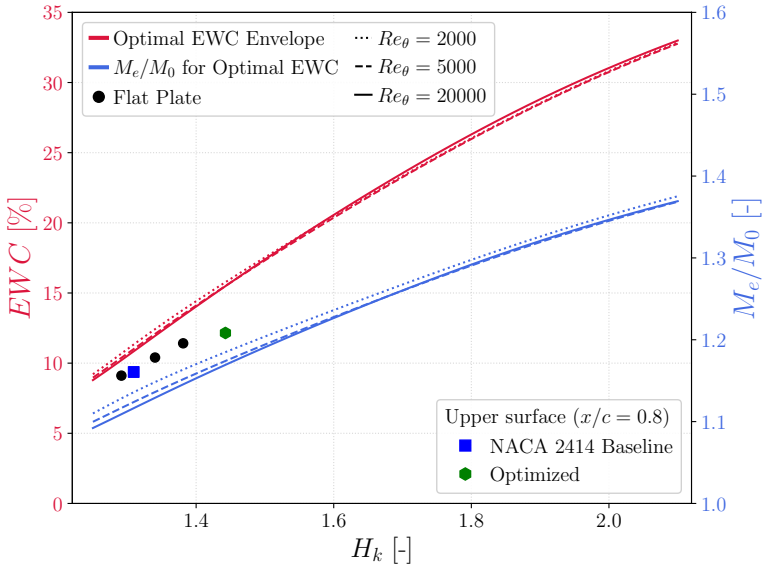
This indicates the existence of an optimal M_e/M_0 value for each H_k that maximizes the EWC, a

relation investigated in Fig. 5. Accordingly, Fig. 5a illustrates the bounding envelope of all iso-M_e/M_0 curves across the examined H_k domain. This maximum EWC envelope is reported in Fig. 5b, which also includes the specific Mach ratios required to achieve these optimal values. While remaining nearly independent of Re_θ, the maximum EWC increases with H_k (and thus with the adverse pressure gradient), rising from 9% at $H_k = 1.25$ to 34% at $H_k = 2.1$. Notably, this optimum is consistently reached for accelerated flows, with the optimal M_e/M_0 increasing from approximately 1.1 at $H_k = 1.25$ to 1.38 at $H_k = 2.1$. It can be pointed out that the optimal EWC curve lies slightly above the flat plate reference points (by roughly 1-2%), suggesting that the maximum recovery potential occurs for flows slightly more accelerated than the zero-pressure-gradient case.

Figure 5b, by providing the maximum reachable EWC contour, generally establishes the theoretical upper bound of the recoverable profile drag fraction for any attached turbulent boundary layer from a thermodynamic perspective. This represents a valuable reference for engineers, guiding boundary-layer-driven designs, such as BLI configurations, and enabling the evaluation of energy recovery efficiency relative to this established limit. However, it must be emphasized that this envelope represents a theoretical limit. In practice, when designing an aircraft, reaching certain regions of this optimal curve may be infeasible, particularly for EWC levels around 20-30%. These peaks correspond to high H_k values, where the boundary layer was subjected to strong adverse pressure gradients. Such conditions may not be physically realizable in conjunction with the high local Mach ratios ($M_e/M_0 \approx 1.3$-1.4 meaning a strongly accelerated flow) required to achieve these optimal recovery levels.



(a) Illustration of EWC envelope construction



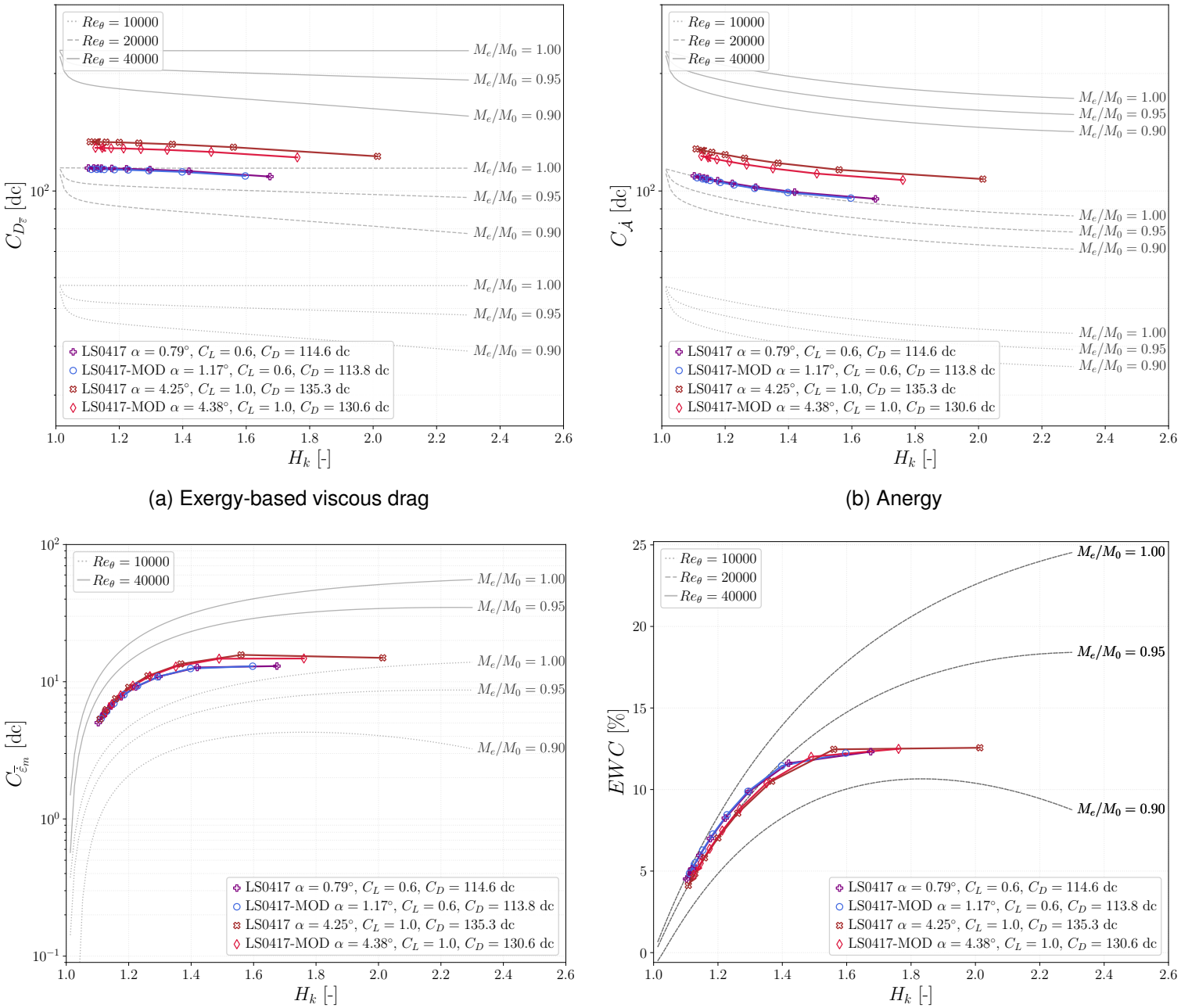
(b) Optimal EWC and associated $\frac{M_e}{M_0}$

Figure 5 – Optimal EWC for turbulent attached boundary layers, $M_0 = 0.3$

3.3 Turbulent Wake

Finally, addressing the turbulent wake, the corresponding exergy characteristic curves, derived using the adapted Coles velocity profile, are presented in Fig. 6. The considered kinematic shape factor (H_k) ranges from 1.0 to 2.3, with momentum thickness Reynolds numbers (Re_θ) of 10000, 20000, and 40000. The edge-to-freestream Mach ratio (M_e/M_0) varies between 0.9 and 1.0. These parameter ranges are representative of wakes developing downstream of attached turbulent boundary layers, corresponding to fully turbulent airfoils operating well below stall incidence.

Along a typical 2D airfoil wake, the maximum H_k and minimum M_e/M_0 values are encountered at the trailing edge. As the wake develops downstream, H_k and M_e/M_0 asymptotically approach unity. This spatial evolution reflects the progressive damping of the wake velocity deficit and the flow's eventual return to unperturbed freestream conditions. As depicted in Fig. 6a, this downstream wake equilibration is accompanied by a slight, continuous increase in the exergy-based viscous drag (C_{D_ξ}),



(a) Exergy-based viscous drag

(b) Anergy

(c) Viscous mechanical exergy

(d) Exergy Waste Coefficient

Figure 6 – Characteristic exergy/IBL curves for turbulent wake at $M_0 = 0.3$ and exergy-based distributions for fully turbulent airfoils at $M_0 = 0.3$, $R_e = 3 \times 10^6$

which accounts for the additional mixing and dissipation occurring within the wake. Consequently, from the trailing edge to the far-field, $C_{D_{\bar{\varepsilon}}}$ exhibits a monotonic increase as H_k decreases and M_e/M_0 rises, ultimately converging toward a constant plateau value along the $M_e/M_0 = 1$ isocontour, which corresponds to the overall profile drag.

Furthermore, like in the laminar case, the exergy-based parameters in the wake ($C_{D_{\bar{\varepsilon}}}$, $\bar{\dot{\varepsilon}}_m$, and $\dot{\mathcal{A}}$) exhibit an exact proportionality with the momentum thickness Reynolds number Re_θ. This scaling translates into perfectly overlapping curves for the Exergy Waste Coefficient (EWC) across the various Re_θ values, as evidenced in Fig. 6d.

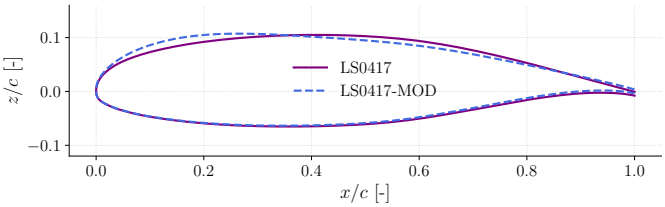
Regarding the exergy decomposition terms $\bar{\dot{\varepsilon}}_m$ and $\dot{\mathcal{A}}$, while they both consistently increase with M_e/M_0, they follow an opposite evolution with H_k. Indeed, as H_k decreases, $\bar{\dot{\varepsilon}}_m$ drops asymptotically toward 0 while $\dot{\mathcal{A}}$ rises. This behavior simply expresses the progressive conversion of viscous exergy into anergy (exergy destruction) through viscous dissipation (an irreversible process). Thus, at an in-

finite location downstream of the body, the profile drag $C_{D_{\bar{\varepsilon}}}$ will consist exclusively of anergy, meaning there is no more recoverable energy fraction. This is expressed by the EWC, which tends to 0 as H_k tends to 1 in Fig. 6d.

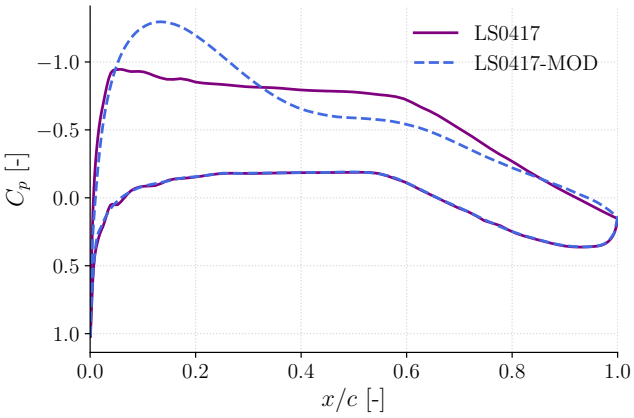
4. Exergy-Based Design Insights for 2D Airfoils

Once the general characteristic maps are established, they can serve as an engineering diagnostic tool by projecting the exergy parameters of specific aerodynamic designs onto the IBL design space. This section presents the practical application of the low-fidelity exergy methodology as a rapid tool for conceptual design, allowing designers to visualize the thermodynamic "trajectories" of existing geometries. Specifically, it enables the identification of which geometry exhibits a higher potential for recoverable viscous exergy ($\bar{\bar{\varepsilon}}_m$) versus non-recoverable anergy generation ($\dot{\mathscr{A}}$), depending on the flight conditions.

To illustrate this, a comparison is made between two closely related general aviation low-speed airfoils, the LS0417 and the LS0417-MOD, focusing on their IBL quantities and associated exergy parameter distributions. As detailed in [14], the LS0417-MOD is a modified version of the baseline LS0417. This modification primarily aims to reduce the pitching moment by increasing the forward loading, and to enhance the climb lift-to-drag ratio by mitigating the adverse pressure gradient on the aft upper surface, as visible in Fig. 7.



(a) Airfoils geometry



(b) Pressure coefficient distributions from XFoil, fully turbulent, $C_L = 0.6$, $M_0 = 0.3$, $Re = 3 \times 10^6$.

Figure 7 – Comparison of the LS0417 and LS0417-MOD airfoils

In the present study, IBL data for the LS0417 and LS0417-MOD airfoils (both featuring a finite trailing-edge thickness of 0.709%) were generated using the XFoil low-fidelity viscous-coupled panel method solver [6]. Transitional cases were computed by setting the critical amplification factor to $N = 9.0$ to predict the natural transition location, whereas fully turbulent conditions were obtained by forcing the transition very close to the leading edge (at $x/c = 1\%$). The two airfoils are compared under two distinct lifting conditions, reflecting cruise and climb operations: lift coefficients of $C_L = 0.6$ and 0.84 are evaluated for the transitional cases, while $C_L = 0.6$ and 1.0 are considered for the fully turbulent ones. The resulting thermodynamic trajectories for the upper surfaces of these airfoils, depicting the evolution of the exergy-based parameters (computed with the low-fidelity method summarized in Fig. 1) as a function of the local H_k encountered along the geometry, are illustrated by colored lines with markers. These trajectories are directly superimposed onto the previously established characteristic curves in Figs. 3, 4, and 6. Along these upper surface trajectories, arrows indicate the downstream flow direction (i.e., increasing x/c). It can be seen how how the local IBL parameters are affected by the geometric modification, which strengthens the adverse pressure gradient near the leading edge while relaxing it toward the trailing edge. Consequently, the modified airfoil exhibits noticeably higher H_k values in the forward region ($0.1 < x/c < 0.4$), as shown in Figs. 3 and 4, while displaying lower H_k values near the trailing edge and into the near-wake ($0.8 < x/c < 1.2$), as depicted in Figs. 4 and 6.

First, regarding the exergy performance in the laminar regions for the transitional cases shown in Fig. 3, where the markers denote chordwise positions at 0.05 increments from $x/c = 0.1$ up to the transition point (x_{tr}/c), it is apparent that the maximum generated profile drag ($C_{D_{\bar{\varepsilon}}}$) and its associated exergy quantities ($\bar{\varepsilon}_m$ and $\dot{\mathscr{A}}$) are encountered at or just before the transition location, where H_k is maximum. Additionally, for such classical airfoils, a significant portion of the profile drag in the laminar zone is potentially recoverable. This is reflected by the high EWC values achieved in this region, which exceed 30% from $x/c > 0.1$ onward, well above the flat plate value.

At $C_L = 0.6$, transition occurs further downstream on the baseline LS0417, ultimately yielding a lower overall profile drag. When comparing the laminar regions of both airfoils, specifically between $x/c \approx 0.2$ and the transition onset of the LS0417-MOD ($x_{tr}/c = 0.28$), the modified geometry exhibits slightly higher levels of $C_{D_{\bar{\varepsilon}}}$, anergy ($\dot{\mathscr{A}}$), and viscous mechanical exergy ($\bar{\varepsilon}_m$) which is directly correlated with locally higher values of the edge velocity (U_e) and the kinematic shape factor (H_k). These elevated parameters are respectively driven by a stronger local flow acceleration (i.e., a lower C_p) and a more severe adverse pressure gradient, both of which result from the increased upper-surface thickness near the leading edge of the modified profile.

At $C_L = 0.84$, the LS0417-MOD airfoil generates a marginally higher overall profile drag ($C_{D_{\bar{\varepsilon}}}$) at the transition point. However, its exergy decomposition reveals a globally lower anergy production ($\dot{\mathscr{A}}$) alongside a higher viscous mechanical exergy ($\bar{\varepsilon}_m$). This translates into a substantially higher EWC for the modified geometry (54% versus 36%). Thus, this exergy-based decomposition provides deeper physical insights beyond the mere evaluation of the overall profile drag. Even though the laminar region of the LS0417-MOD profile generates slightly more drag from a classical aerodynamic perspective, the exergy analysis reveals that it actually presents a significantly higher potential for recoverable mechanical power when coupled with a propulsion system.

Furthermore, the upper-surface exergy distributions within the turbulent boundary layer for the fully turbulent cases are presented in Fig. 4. Once again, arrows indicate the downstream flow direction, this time from $x/c = 0.1$ to $x/c = 0.9$, with markers denoting chordwise stations at $\Delta x/c = 0.1$ increments.

It is noteworthy that the local $C_{D_{\bar{\varepsilon}}}$ values in the aft region ($0.7 < x/c < 0.9$) are marginally higher for the LS0417-MOD, even though it ultimately yields a slightly lower overall profile drag. Focusing on this aft region at $C_L = 0.6$, this locally elevated drag translates into concurrently higher values for both anergy ($\dot{\mathscr{A}}$) and viscous mechanical exergy ($\bar{\varepsilon}_m$), which results in an EWC level similar to that of the baseline LS0417 airfoil. However, at $C_L = 1.0$, the slight drag increase for the LS0417-MOD in this same region is almost exclusively driven by a rise in anergy, the viscous mechanical exergy remaining roughly constant between the two airfoils, which ultimately results in a lower EWC value for the modified profile at $x/c = 0.9$ (17.0% versus 18.6% for the baseline).

Conversely, if the objective is to maximize the available energy recovery potential between $x/c = 0.4$ and 0.5, the LS0417-MOD proves more advantageous, exhibiting higher EWC values than the baseline profile (e.g., 14.9% versus 12.2% at $x/c = 0.4$). Finally, it is interesting to note that the EWC levels reached near mid-chord ($x/c \approx 0.5$) closely approach the thermodynamic EWC limit established in Fig. 5. This indicates that these mid-chord regions offer very little margin for further optimization in terms of energy recovery, unlike the flow near the trailing edge, which remains far from this optimum.

Finally, the exergy distributions within the turbulent wake for the fully turbulent cases are presented in Fig. 6. Once again, arrows indicate the downstream flow direction, this time from $x/c = 1.2$ to $x/c = 1.8$, with markers denoting wake stations at $\Delta x/c = 0.1$ increments. First, for the climb condition (at $C_L = 1.0$), it is verified that the exergy-based profile drag is slightly lower for the modified airfoil. This yields an improved climb lift-to-drag ratio of approximately 6%, which is consistent with the values reported in [14].

Overall, at $C_L = 0.6$, both airfoils exhibit nearly identical levels of profile drag ($C_{D_{\bar{\varepsilon}}}$), alongside matching decompositions into anergy ($\dot{\mathscr{A}}$) and viscous mechanical exergy ($\bar{\varepsilon}_m$). Consequently, their respective EWC trajectories are almost perfectly superimposed. At $C_L = 1.0$, despite the baseline LS0417 exhibiting noticeably higher H_k values near the trailing edge, both profiles initially present very similar $C_{D_{\bar{\varepsilon}}}$ values in the near-wake ($x/c = 1.1$). This difference becomes more pronounced further downstream, with the LS0417-MOD ultimately generating less drag (a reduction of approximately 4.5 drag

counts by $x/c = 1.8$). Because this overall drag reduction is evenly distributed between lower mechanical exergy and lower anergy, the resulting EWC levels remain similar for both airfoils throughout the wake, as evidenced by their overlapping curves.
Furthermore, one can observe that the higher lift condition ($C_L = 1.0$) induces a more rapid decay of mechanical exergy and a correspondingly faster dissipation into anergy along the wake as evidenced in the EWC plots. This suggests that energy recovery via downstream wake ingestion (here for $x/c > 1.2$) would be less efficient behind such airfoils when operating at higher lifting conditions.
To summarize, regarding the upper-surface exergy metrics of these airfoils, the LS0417-MOD generally presents a greater energy recovery potential within the laminar boundary layer for the transitional cases, as well as near mid-chord for the fully turbulent cases. Conversely, when approaching the trailing edge under climb conditions (i.e., at $C_L = 1.0$ within the $0.8 < x/c < 1.0$ region), it exhibits a lower energy recovery potential than the baseline profile. Finally, further downstream in the near-wake, both airfoils preserve a similar energy recovery potential.
Beyond evaluating the thermodynamic performance of existing geometries, these characteristic maps can facilitate a rapid inverse design logic. A target EWC level can, for instance, be directly linked to the required local boundary layer state, defined by H_k, M_e/M_0, and Re_θ. Given its low computational cost, this approach serves as a highly practical tool to drive aerodynamic optimization processes during the early design phases. Such an optimization procedure will be addressed in the following section.

5. Low-Fidelity Exergy-Driven Airfoil Shape Optimization

Although several entropy-based shape optimization frameworks exist in the literature [15, 16, 4], these approaches invariably rely on mid-fidelity RANS simulations, which often prove computationally prohibitive during the conceptual design phase. Conversely, traditional 2D airfoil optimization strategies based on low-fidelity panel methods [17, 18] focus almost exclusively on global aerodynamic targets, such as the lift, drag, and pitching moment coefficients. To bridge this gap, this section introduces a rapid, exergy-driven airfoil optimization methodology suitable for conceptual design, which leverages the low-fidelity exergy formulation [5] (summarized in Fig. 1) applied to local IBL parameters from viscous-coupled panel method solutions.
Recently, Collazo [19] introduced an insightful airfoil design framework driven by local IBL parameters rather than global aerodynamic loads. While their method fundamentally relies on classical momentum analysis, such as minimizing the trailing-edge momentum thickness θ, the present objective is instead to define an objective function that directly depends on exergy metrics evaluated through the low-fidelity formulation.

5.1 Genetic Algorithm and Optimization Loop Methodology

While Collazo [19] utilizes an inverse design method based on target pressure distributions (C_p), the corresponding inverse design modules, such as the one embedded in XFoil, prove rather impractical to implement within fully automated optimization loops. Instead, a more general and versatile Genetic Algorithm (GA) approach is adopted here, as widely employed in the literature for 2D airfoil design [15],[20], [16], [18]. Although GAs do not provide a rigorous mathematical proof of global optimality, they efficiently explore the design space and avoid local minima. This global exploration capability makes them a particularly suitable choice when the number of design variables remains limited, as in the present 2D case.
To drive the GA, a parameterization of the airfoil shape is required. The PARSEC method is adopted in this study, aligning with similar 2D airfoil optimization applications [20], [17], [18]. This approach offers the advantage of describing the profile geometry through a concise set of 11 intuitive geometrical parameters (e.g., leading-edge radius, maximum thickness, and its corresponding chordwise location). Further details regarding parameterization techniques can be found in [21].
The adopted optimization methodology proceeds through the following key steps:

1. The baseline airfoil geometry is first converted and fitted using the 11 PARSEC geometrical parameters. An initial population consisting of X individuals is then randomly generated around this baseline parameterization.

2. Each individual airfoil within the population is analyzed using XFoil. The resulting IBL parameters are extracted and supplied to the low-fidelity exergy method to evaluate the objective fitness score. The fitness function driving the optimization is defined as:

$$\mathscr{F} = \Delta EWC - \lambda \cdot \max(\Delta C_D, 0) \tag{11}$$

where ΔEWC represents the improvement in the Exergy Waste Coefficient over a targeted spatial region of the geometry, and ΔC_D denotes the change in the overall profile drag. The penalty term involving the weighting factor λ (λ>0) is specifically designed to penalize any drag increase without rewarding drag reduction. Consequently, the primary objective of this exergy-driven framework is to maximize the airfoil's thermodynamic performance (i.e., maximizing the available viscous mechanical exergy for propulsion integration purposes) while maintaining the baseline global aerodynamic loads (C_L and C_D).

3. Based on the computed fitness scores, the best-performing individuals are selected using a combination of elitism and tournament selection strategies. Genetic operators (crossover and mutation) are subsequently applied to these selected individuals to produce the next generation of airfoils.

4. The newly generated population undergoes the same XFoil evaluation and exergy-based fitness scoring process. This continuous loop is iterated until the predefined maximum number of generations (N) is reached. Ultimately, the individual exhibiting the highest fitness score across the entire process is returned as the final optimized design.

This overall workflow associated with this exergy-based optimization methodology is summarized in Fig. 8.

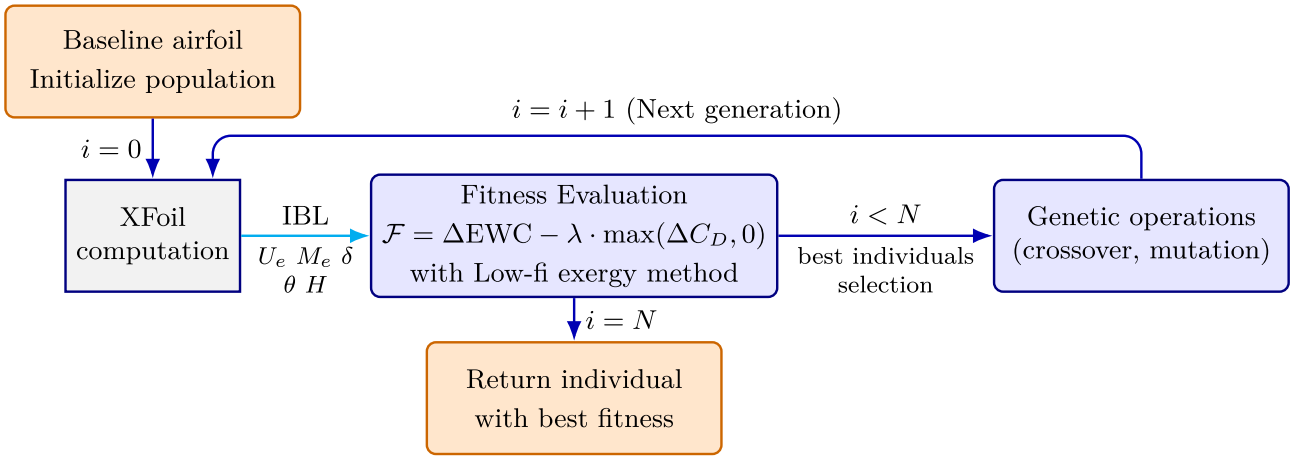


Figure 8 – Low-fidelity exergy-driven optimization framework using a genetic approach.

5.2 Exergy Optimization of the NACA 2414 Airfoil

This section presents the application of the previously described methodology to the exergy optimization of a fully turbulent NACA 2414 airfoil. The optimization is conducted at a target lift coefficient of $C_L = 0.6$, at a Reynolds number of $Re = 3 \times 10^6$, and freestream Mach number of $M_0 = 0.3$, with boundary layer transition fixed at $x/c = 1\%$. This specific airfoil case was also studied by Krishnan [18], and the initial baseline PARSEC parameters were extracted from Table 1 of this work.

For 2D airfoils, the upper surface plays the predominant role in dictating the net aerodynamic loads. Consequently, this region also exhibits the highest amount of available viscous exergy along the profile. For this reason, the present study focuses exclusively on the exergy optimization of the airfoil's upper surface.

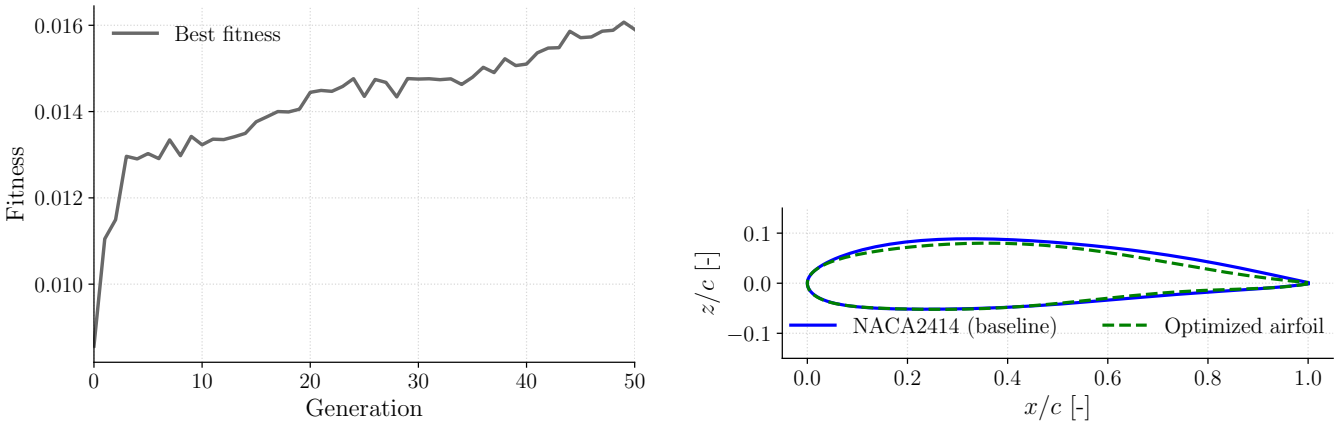
In practice, the objective function targets the mean EWC over a specific chordwise region rather than at a single point, which avoids discontinuities and non-physical behavior in boundary layer parameters. Here, the target region is set between $x/c = 0.7$ and 0.9 on the upper surface. The underlying

idea is to simulate a Boundary Layer Ingestion (BLI) configuration, where flow ingestion is typically performed at the rear of the body, as evidenced in the Blended Wing Body (BWB) test case studied by Arntz [1]. A penalty coefficient of $\lambda = 20$ is chosen to strictly penalize any overall drag increase while the lift coefficient is constrained to $C_L = 0.6$ by imposing it directly within the XFoil computations. Regarding the genetic algorithm parameters, a population size of $X = 25$ and a number of generations of $N = 50$ were chosen, consistent with the setup adopted in [20].

The overall optimization process required approximately 2500 seconds on an ARM-based M2 processor, utilizing a single-core configuration without parallel computing. As shown in Fig. 9a, the fitness score rises rapidly during the initial generations before improving more gradually. Although strict convergence is not fully reached at $N = 50$, this limit is deemed satisfactory, as preliminary tests demonstrated no notable improvement with a significantly higher number of iterations.

A geometrical comparison between the resulting optimized airfoil and the baseline is presented in Fig. 9b. The optimized upper surface is slightly thinner, and more notably, the position of maximum thickness is shifted further aft. This modification induces a steeper slope in the rear portion of the upper surface, resulting in a stronger adverse pressure gradient.

The global aerodynamic loads and exergy performance metrics are summarized in Table 1. To maintain the constrained lift coefficient of $C_L = 0.6$, the optimized airfoil requires a higher angle of attack (an increase of approximately $0.9°$). Furthermore, the optimization successfully yields a slight drag reduction (-1.6 drag counts) while effectively improving the mean EWC over the targeted upper surface region ($0.7 < x/c < 0.9$) by approximately 2.3%.



(a) Genetic algorithm convergence history

(b) Airfoil geometry comparison

Figure 9 – Optimization result for the fully turbulent NACA 2414, $C_L = 0.6$, $M_0 = 0.3$, $Re = 3 \times 10^6$.

Airfoil	α (°)	C_L	C_D (dc)	Mean EWC (%) (upper surface, $0.7 < x/c < 0.9$)
Baseline	3.19	0.6	105.7	9.35
Optimized	4.04	0.6	104.1	11.64

Table 1 – Comparison of aerodynamic loads and exergy metrics for the baseline NACA 2414 and exergy-optimized airfoils, fully turbulent, $M_0 = 0.3$, $Re = 3 \times 10^6$.

Figure 10 compares the detailed distributions along the chord of the IBL parameters (H_k, Re_θ, as well as U_e linked to the C_p field) between the initial baseline airfoil and the optimized one. Meanwhile, Fig. 11 compares the associated exergy-based parameters.

First, regarding the IBL parameters, it is observed that the optimized profile presents a noticeably higher shape factor than the baseline in the optimization target region ($0.7 < x/c < 0.9$). This is caused by the stronger adverse pressure gradient in this region, which also has a thickening effect on the boundary layer, with a higher Re_θ in this zone. On the other hand, there is a slight decrease in U_e due to the locally higher pressure coefficient.

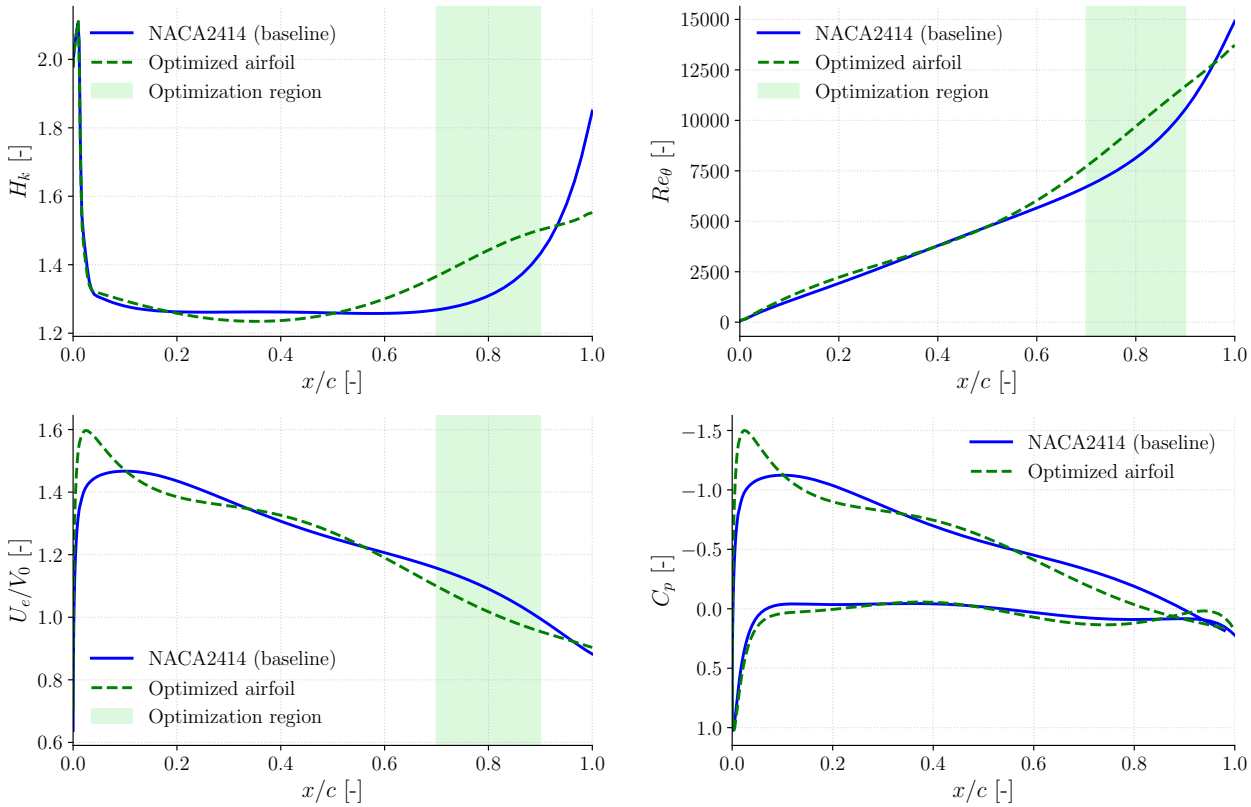
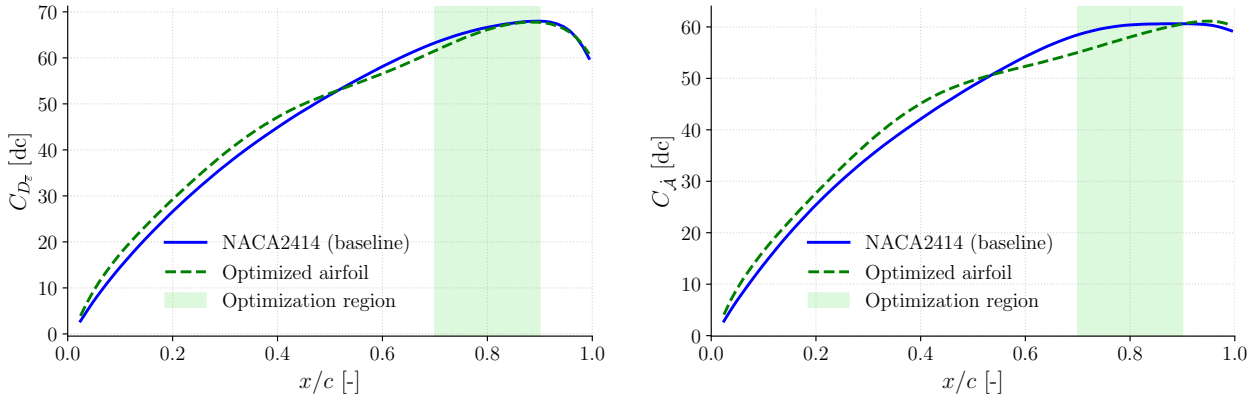
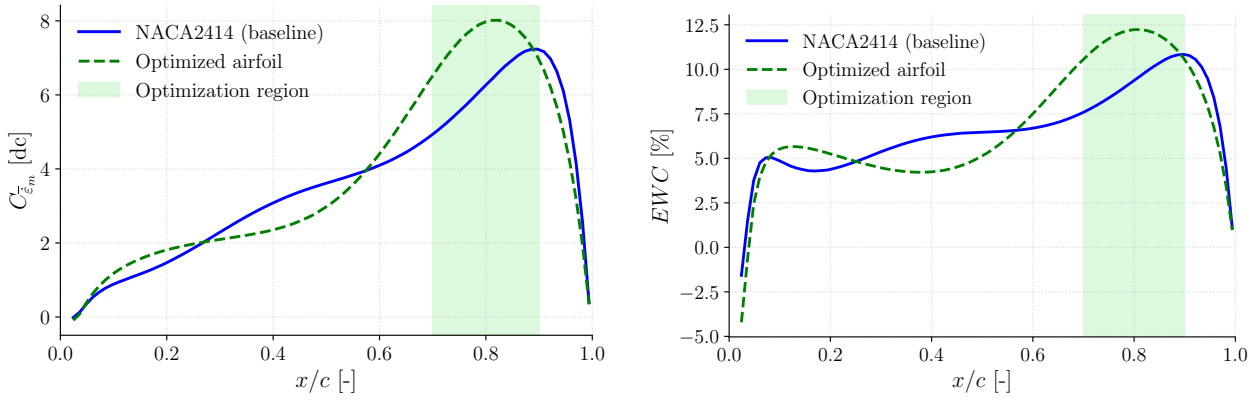


Figure 10 – Comparison of upper-surface integral boundary layer parameters for the baseline NACA 2414 and the exergy-optimized airfoil, $C_L = 0.6$, $M_0 = 0.3$, $Re = 3 \times 10^6$.



(a) Exergy-based viscous drag

(b) Anergy



(c) Viscous mechanical exergy

(d) Exergy Waste Coefficient

Figure 11 – Comparison of upper-surface exergy distributions for the baseline NACA 2414 and the exergy-optimized airfoil, $C_L = 0.6$, $M_0 = 0.3$, $R_e = 3 \times 10^6$.

These boundary layer parameter modifications result in a notable increase in the EWC in the target region, which is the objective quantity of the optimization. Notably, a maximum of approximately 12.2% is reached at $x/c = 0.8$, versus about 9.4% for the baseline, as seen in Fig. 11d. This rise in EWC is well characterized by a local increase in $\bar{\varepsilon}_m$ (see Fig. 11c) and, therefore, of the recoverable fraction of profile drag exploitable through integrated propulsion. In the meantime, there is a reduction in anergy (Fig. 11b) locally in this region. Overall, this results in a profile drag $C_{D_{\bar{\varepsilon}}}$ distribution that does not change much in this target region. These obtained EWC levels are also compared to the theoretical limits in Fig. 5b by superimposing the data points from the $x/c = 0.8$ location. Despite the increases from the baseline to the optimized airfoil, the baseline configuration actually operates closer to the theoretical optimum for its corresponding H_k. In contrast, the optimized profile deviates further from the theoretical maximum at its new H_k value. This shift is primarily due to a decrease in the local edge Mach number ratio (M_e/M_0) for the optimized airfoil, which moves it further away from the optimal M_e/M_0 condition.
Thus, it is illustrated here that while the baseline and modified airfoils have globally maintained similar aerodynamic characteristics from the perspective of a classical momentum approach (overall loads C_L, C_D), the further thermodynamic decomposition appears to be the dedicated tool to drive the optimization of power savings achievable through airframe/system coupling.

6. Conclusions

A comprehensive link between exergy and classical Integral Boundary Layer (IBL) parameters for steady, attached, subsonic flows has been established through the construction of characteristic curves using a low-fidelity exergy method. This approach enables the systematic prediction of the thermodynamic performance of any laminar or turbulent boundary layer and wake state, covering a wide aircraft design space.
Then, the characterization of the LS0417 low-speed airfoil family demonstrated the value of exergy metrics as a powerful conceptual design tool for evaluating and comparing the propulsive integration potential of different geometries. Notably, this study highlighted that the optimal airfoil choice is highly dependent on the targeted recovery location, the boundary layer regime (laminar or turbulent), and the specific flight conditions (e.g., cruise versus climb).
Finally, a novel low-fidelity, exergy-driven airfoil shape optimization framework based on a genetic algorithm was developed. Targeting the maximization of the recoverable exergy fraction within the profile drag, this method was successfully applied to a NACA 2414 airfoil. The results demonstrated its capability to yield an optimized design that maintains baseline aerodynamic loads (C_L, C_D) while significantly enhancing the power recovery margin.
Future work should explore versatile parameterizations for complex shapes and integrate multipoint optimization to ensure robust performance across multiple flight conditions. Ultimately, applying this framework to actual Boundary Layer Ingestion (BLI) configurations will demonstrate its full potential.

7. Acknowledgments

The authors would like to thank Aura Aero and the National Higher French Institute of Aeronautics and Space for supporting this research. The authors also wish to acknowledge Megha Dinesh, a Master's student at ISAE-SUPAERO, for her contribution to the implementation of the exergy optimization framework based on a genetic approach presented in this work.

8. Contact Author Email Address

The contact author for this paper is Guillaume Bourreau-Tirel (PhD Candidate).
Email: guillaume.bourreautirel@aura-aero.com

9. Copyright Statement

The authors confirm that they, and/or their company or organization, hold copyright on all of the original material included in this paper. The authors also confirm that they have obtained permission, from the copyright holder of any third party material included in this paper, to publish it as part of their paper. The authors confirm that they give permission, or have obtained permission from the copyright holder of this paper, for the publication and distribution of this paper as part of the ICAS proceedings or as individual off-prints from the proceedings.

References

[1] Arntz A. Civil aircraft aero-thermo-propulsive performance assessment by an exergy analysis of high-fidelity CFD-RANS flow solutions. Ph.D. dissertation, Université de Lille 1, 2014.

[2] Aguirre MA, Duplaa S, Carbonneau X and Turnbull A. Velocity decomposition method for exergy-based drag prediction. *AIAA Journal*, Vol. 58, No. 11, pp 4686–4701, 2020.

[3] Lamprakis I and Sanders DS. Defect force and viscous mechanical energy generation in aerodynamic flows. *Journal of Aircraft*, pp 1–23, 2025.

[4] Novotny N. An exergy approach for high-fidelity analysis and optimization of aerospace systems. Ph.D. Dissertation, University of Dayton, 2024.

[5] Bourreau-Tirel G, Duplaa S, Aguirre MA and Ruscio JP. Low-fidelity exergy-based method for profile drag analysis. *AIAA Journal*, Vol. 64, No. 4, pp 2142–2159, 2026.

[6] Drela M. XFOIL: An analysis and design system for low Reynolds number airfoils., 1989.

[7] Whitfield DL. Integral solution of compressible turbulent boundary layers using improved velocity profiles. Final Report, Mar. - Nov. 1977 ARO, Inc., Arnold Air Force Station, TN., 1978.

[8] Drela M. Power balance in aerodynamic flows. *AIAA Journal*, Vol. 47, No. 7, pp 1761–1771, 2009.

[9] Drela M. *Flight vehicle aerodynamics*. MIT Press, Cambridge, MA, 2014.

[10] Clauser FH. Turbulent boundary layers in adverse pressure gradients. *Journal of the Aeronautical Sciences*, Vol. 21, No. 5, pp 91–108, 1954.

[11] Swafford TW. Analytical approximation of two-dimensional separated turbulent boundary-layer velocity profiles. *AIAA Journal*, Vol. 21, No. 6, pp 923–926, 1983.

[12] Bourreau-Tirel G, Duplaa S and Aguirre MA. Exergy-based aerodynamic analysis methodology for low-fidelity aircraft design. *TSAS 3AF Conference*, Toulouse, France, 2025.

[13] Lamprakis L, Sanders DS and Laskaridis P. Fundamental concepts of boundary-layer ingestion propulsion. *Journal of Aircraft*, Vol. 62, No. 5, pp 1182–1203, 2025.

[14] McGhee RJ and Beasley WD. Wind-tunnel results for a modified 17-percent-thick low-speed airfoil section. NTRS Document ID: 19820003160, November 1981.

[15] Li H and Figliola R. Exergy based design methodology for airfoil shape optimization. *10th AIAA/ISSMO Multidisciplinary Analysis and Optimization Conference*, 2004.

[16] Wang W, Wang J, Yang XP and Ding YY. Aerodynamic optimization design of airfoil shape using entropy generation as an objective. *Journal of Thermal Science and Engineering Applications*, Vol. 11, No. 021015, 2018.

[17] Belda M and Hyhlík T. Interactive airfoil optimization using parsec parametrization and adjoint method. *Applied Sciences*, Vol. 14, No. 8, p 3495, 2024.

[18] Krishnan A, Al-Obaidi ASM and Ching Hao L. Optimizing NACA2414 airfoil aerodynamics with PARSEC parametrization and genetic algorithm. *E3S Web of Conferences*, Vol. 514, p 03004, 2024.

[19] Collazo Garcia AR and Ansell PJ. Airfoil design framework for optimized boundary-layer integral parameters. *Journal of Aircraft*, Vol. 61, No. 5, pp 1412–1427, 2024.

[20] Della Vecchia P, Daniele E and D'Amato E. An airfoil shape optimization technique coupling PARSEC parameterization and evolutionary algorithm. *Aerospace Science and Technology*, Vol. 32, No. 1, pp 103–110, 2014.

[21] Salunke NP, Ahamad RAJ and Channiwala SA. Airfoil parameterization techniques: a review. *American Journal of Mechanical Engineering*, Vol. 2, No. 4, pp 99–102, 2014.